A&A 664, A33 (2022)
https://doi.org/10.1051/0004-6361/202243484

Astronomy & Astrophysics

Four sub-Jovian-mass planets detected by high-cadence microlensing surveys

Cheongho Han[1], Doeon Kim[1], Andrew Gould[2,3], Andrzej Udalski[4], Ian A. Bond[5], Valerio Bozza[6], Youn Kil Jung[7], Michael D. Albrow[8], Sun-Ju Chung[7], Kyu-Ha Hwang[7], Yoon-Hyun Ryu[7], In-Gu Shin[7], Yossi Shvartzvald[9], Jennifer C. Yee[10], Weicheng Zang[11], Sang-Mok Cha[7,12], Dong-Jin Kim[7], Seung-Lee Kim[7], Chung-Uk Lee[7], Dong-Joo Lee[7], Yongseok Lee[7,13], Byeong-Gon Park[7,13], Richard W. Pogge[3]
(The KMTNet Collaboration)
Przemek Mróz[4], Michał K. Szymański[4], Jan Skowron[4], Radosław Poleski[4], Igor Soszyński[4], Paweł Pietrukowicz[4], Szymon Kozłowski[4], Krzysztof Ulaczyk[14], Krzysztof A. Rybicki[4], Patryk Iwanek[4]
(The OGLE Collaboration)
Fumio Abe[15], Richard K. Barry[15], David P. Bennett[17,18], Aparna Bhattacharya[17,18], Hirosane Fujii[15], Akihiko Fukui[19,20], Yuki Hirao[16,17,21], Yoshitaka Itow[15], Rintaro Kirikawa[21], Naoki Koshimoto[21], Iona Kondo[21], Yutaka Matsubara[15], Sho Matsumoto[21], Shota Miyazaki[21], Yasushi Muraki[21], Greg Olmschenk[22], Arisa Okamura[21], Clément Ranc[23], Nicholas J. Rattenbury[24], Yuki Satoh[21], Stela Ishitani Silva[17,25], Takahiro Sumi[21], Daisuke Suzuki[26], Taiga Toda[21], Paul J. Tristram[27], Aikaterini Vandorou[22], and Hibiki Yama[21]
(The MOA Collaboration)

(Affiliations can be found after the references)

Received 5 March 2022 / Accepted 23 May 2022

ABSTRACT

Aims. With the aim of finding short-term planetary signals, we investigated the data collected from current high-cadence microlensing surveys.
Methods. From this investigation, we found four planetary systems with low planet-to-host mass ratios, including OGLE-2017-BLG-1691L, KMT-2021-BLG-0320L, KMT-2021-BLG-1303L, and KMT-2021-BLG-1554L. Despite the short durations, ranging from a few hours to a couple of days, the planetary signals were clearly detected by the combined data of the lensing surveys. We found that three of the planetary systems have mass ratios on the order of 10^{-4} and the other has a mass ratio that is slightly greater than 10^{-3}.
Results. The estimated masses indicate that all discovered planets have sub-Jovian masses. The planet masses of KMT-2021-BLG-0320Lb, KMT-2021-BLG-1303Lb, and KMT-2021-BLG-1554Lb correspond to ~0.10, ~0.38, and ~0.12 times the mass of the Jupiter, and the mass of OGLE-2017-BLG-1691Lb corresponds to that of the Uranus. The estimated mass of the planet host KMT-2021-BLG-1554L, $M_{\rm host} \sim 0.08\,M_\odot$, corresponds to the boundary between a star and a brown dwarf. Besides this system, the host stars of the other planetary systems are low-mass stars with masses in the range of ~[0.3–0.6] $M_\odot$. The discoveries of the planets fully demonstrate the capability of the current high-cadence microlensing surveys in detecting low-mass planets.

Key words. planets and satellites: detection – gravitational lensing: micro

1. Introduction

During the 2010s, microlensing entered an era of high-cadence surveys with the instrumental upgrade of previously established experiments and the participation of a new experiment. The new era started with the Microlensing Observations in Astrophysics survey (MOA: Bond et al. 2001), which had previously carried out a lensing survey using a 0.61 m telescope and a camera with a 1.3 deg^2 field of view (FOV) during the early phase, launching its second phase experiment with the employment of a 1.8 m telescope equipped with a wide-field camera yielding a 2.2 deg^2 FOV. Since its first operation in 1992, the Optical Gravitational Lensing Experiment (OGLE) has been upgraded multiple times, and it is in its fourth phase (OGLE-IV: Udalski et al. 2015) with the employment of a 1.3 m telescope and a camera with a 1.4 deg^2 FOV. The Korea Microlensing Telescope Network (KMTNet: Kim et al. 2016), which was launched in 2016, is being carried out with the use of three globally distributed 1.6 m telescopes, each of which is mounted with a wide-field detector providing a 4 deg^2 FOV. With the use of wide-field cameras mounted on multiple telescopes, the current lensing surveys can monitor lensing events with a dramatically enhanced observational cadence.

The greatly increased observational cadence of the lensing surveys has brought out important changes not only in the observational strategy but also in the outcome of planetary microlensing searches. First, being able to resolve short-lasting planetary signals from survey observations, the high-cadence surveys can function without the survey+followup experiment mode, in which low-cadence surveys mainly detect and alert

Table 1. Coordinates, fields, alert dates, and baseline magnitudes.

Event	$(RA, Dec)_{J2000}$	(l, b)	Field	Alert date	I_{base} (mag)
OGLE-2017-BLG-1691 (KMT-2017-BLG-0752)	(17:34:22.52, –29:17:05.39)	(−1°.601, 1°.895)	OGLE (BLG654.31) KMT (BLG14)	2017 Sep. 6 postseason	19.90
KMT-2021-BLG-0320	(17:57:33.15, –30:30:14.18)	(2°.095, −4°.299)	KMT (BLG01, BLG41)	2021 Apr. 9	20.08
KMT-2021-BLG-1303 (MOA-2021-BLG-182)	(18:07:27.33, –29:16:53.69)	(−0°.027, −3°.028)	KMT (BLG04) MOA (gb13)	2021 Jun. 14 2021 Jun. 17	19.67
KMT-2021-BLG-1554	(17:51:12.82, –31:51:51.70)	(−1°.888, −2°.543)	KMT (BLG01, BLG41)	2021 Jul. 1	22.39

Notes. HJD′ = HJD − 2 450 000.

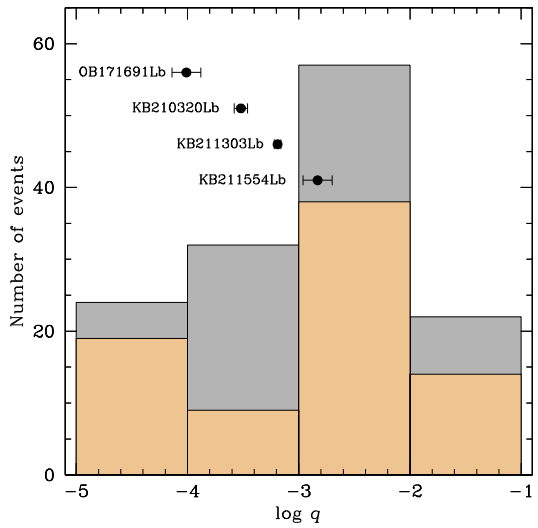

Fig. 1. Histogram of published microlensing planets as a function of the planet-to-host mass ratio. The histogram of planets detected with the data from KMTNet survey is separately marked in brown. The solid dots with error bars indicate the four planets reported in this work.

lensing events and followup groups densely observe the alerted events. Second, the number of microlensing planets has substantially increased with the operation of the high-cadence surveys. Among the total 135 microlensing planets with measured mass ratios[1], 80 (59%) planets were found with the use of the data from the KMTNet survey. This can be seen in Fig. 1, in which we present the histogram of microlensing planets as a function of the planet-to-host mass ratio q. The histogram also shows that the high-cadence surveys contribute to the detections of planets with very low mass ratios, especially those with $q < 10^{-4}$.

In this paper, we report four planetary systems with low planet-to-host mass ratios detected from the microlensing surveys. Despite the short durations (ranging from a few hours to a couple of days), the planetary signals were clearly detected by the combined data of the lensing surveys. It is found that all of the discovered planets have sub-Jovian masses lying in the range of [0.05–0.38] M_J, illustrating the importance of the high-cadence surveys in detecting low-mass planets.

We present the analysis of the planetary lensing events according to the following organization. In Sect. 2, we describe the observations of the individual lensing events, instrument used for observations, and the process of the data reduction. In Sect. 3, we explain the procedure of analysis that is applied to each of the individual events. In the subsequent subsections, we describe the detailed features of the planetary signals and present the results of the analyses conducted for the individual lensing events. In Sect. 4, we specify the types of the source stars and estimate the angular Einstein radii of the lens systems. In Sect. 5, we estimate the physical parameters of the planetary systems by conducting Bayesian analyses. We summarize the results of the analyses and present our conclusions in Sect. 6.

2. Observations and data

The four lensing events for which we present analyses are (1) OGLE-2017-BLG-1691 (KMT-2017-BLG-0752), (2) KMT-2021-BLG-0320, (3) KMT-2021-BLG-1303 (MOA-2021-BLG-182), and (4) KMT-2021-BLG-1554. The source stars of all the events lie toward the Galactic bulge field. In Table 1, we list the equatorial and galactic coordinates, observation fields of the surveys, alert dates, and baseline magnitudes of the individual events. The baseline magnitude I_{base} is approximately scaled to the OGLE-III photometry system.

The events were detected from the combined observations of the lensing surveys conducted by the KMTNet, OGLE, and MOA groups. The KMTNet survey utilizes three identical 1.6 m telescopes that are distributed in three countries of the Southern Hemisphere for the continuous coverage of lensing events. The sites of the individual telescopes are the Siding Spring Observatory in Australia (KMTA), the Cerro Tololo InterAmerican Observatory in Chile (KMTC), and the South African Astronomical Observatory in South Africa (KMTS). Observations by the OGLE survey were conducted using the 1.3 m telescope located at Las Campanas Observatory in Chile. The MOA survey uses the 1.8 m telescope at the Mt. John Observatory in New Zealand. Observations were done mainly in the I band for the KMTNet and OGLE surveys and in the customized MOA-R band for the MOA survey. A subset of images were acquired in the V band for the purpose of estimating source colors. The detailed procedure of the source color estimation is discussed in Sect. 4.

[1] The sample includes 119 planets listed in the NASA Exoplanet Archive (https://exoplanetarchive.ipac.caltech.edu/index.html) plus 16 planets that are not included in the archive: KMT-2020-BLG-0414Lb (Zang et al. 2021a), OGLE-2019-BLG-1053Lb (Zang et al. 2021b), KMT-2019-BLG-0253Lb, KMT-2019-BLG-0953Lb, OGLE-2018-BLG-0977Lb, OGLE-2018-BLG-0506Lb, OGLE-2018-BLG-0516Lb, OGLE-2019-BLG-1492Lb (Hwang et al. 2022), KMT-2017-BLG-2509Lb, OGLE-2017-BLG-1099Lb, OGLE-2019-BLG-0299Lb (Han et al. 2021), OGLE-2016-BLG-1093Lb (Shin et al. 2022), KMT-2018-BLG-1988Lb (Han et al. 2022b), KMT-2021-BLG-0912Lb (Han et al. 2022a), OGLE-2019-BLG-0468Lb, and OGLE-2019-BLG-0468Lc (Han et al. 2022c).

Table 2. Error bar readjustment factors.

Event	Data set	k	$\sigma_{\rm min}$ (mag)
OGLE-2017-BLG-1691	OGLE	1.010	0.010
	KMTA	0.866	0.040
	KMTC	1.170	0.010
	KMTS	1.131	0.020
KMT-2021-BLG-0320	KMTA (BLG01)	1.127	0.040
	KMTA (BLG41)	1.389	0.025
	KMTC (BLG01)	1.091	0.020
	KMTC (BLG41)	1.175	0.020
	KMTS (BLG01)	1.356	0.010
	KMTS (BLG41)	1.319	0.010
KMT-2021-BLG-1303	KMTA	1.304	0.020
	KMTC	1.237	0.010
	KMTS	1.364	0.010
	MOA	1.034	0.020
KMT-2021-BLG-1554	KMTA (BLG01)	1.371	0.020
	KMTA (BLG41)	1.446	0.020
	KMTC (BLG01)	1.418	0.020
	KMTC (BLG41)	1.367	0.020
	KMTS (BLG41)	1.364	0.020

The reduction and photometry of the data were done using the pipelines of the individual survey groups: Albrow et al. (2009) for the KMTNet survey, Woźniak (2000) for the OGLE survey, and Bond et al. (2001) for the MOA survey. All these pipelines apply the difference image analysis algorithm (Tomaney & Crotts 1996; Alard & Lupton 1998) developed for the optimal photometry of stars lying in very dense star fields. For a subset of the KMTC data set, we carried out additional photometry utilizing the pyDIA code (Albrow 2017) for the specification of the source colors. Following the routine described in Yee et al. (2012), we rescale the error bars of data by $\sigma = k(\sigma^2_{\rm min} + \sigma^2_0)^{1/2}$, where σ_0 represents the error estimated from the photometry pipeline, $\sigma_{\rm min}$ is a factor used to make the data consistent with the scatter of data, and the factor k is used to make χ^2 per degree of freedom for each data set become unity. In Table 2, we list the factors k and $\sigma_{\rm min}$ of the individual data sets.

3. Analyses

The light curves of the analyzed events share a common characteristic that short-lived anomalies appear on the otherwise smooth and symmetric form of a single-lens single-source (1L1S) event. Such anomalies in lensing light curves can be produced by two channels, in which the first channel is a perturbation induced by a low-mass companion, such as a planet, to the lens (Gould & Loeb 1992), and the second channel is an anomaly caused by a faint companion to the source (Gaudi 1998). Hereafter, we denote events with a binary lens and a binary source as 2L1S and 1L2S events, respectively. We examine the origins of the anomalies by modeling the light curve of the individual events under these 2L1S and 1L2S interpretations.

Lensing light curves are described by the combination of various lensing parameters. For a 1L1S event, the light curve is described by three parameters of $(t_0, u_0, t_{\rm E})$, which denote the time of the closest approach of the source to the lens, the separation (scaled to the angular Einstein radius $\theta_{\rm E}$) between the source and lens at that time, and the time scale of the event, respectively. The event time scale is defined as the time required for a source to transit $\theta_{\rm E}$.

In addition to these basic parameters, describing the light curve of a 2L1S event requires one to include extra parameters of (s, q, α), which represent the separation (scaled to $\theta_{\rm E}$) and mass ratio between the binary lens components, and the angle between the binary-lens axis and the direction of the source motion (source trajectory angle), respectively. Because planet-induced anomalies are usually generated by the crossings over or close approach of the source to the planet-induced caustics, an additional parameter of the normalized source radius ρ, which is defined as the ratio of the angular radius of the source θ_* to $\theta_{\rm E}$, is needed to describe the deformation of the anomaly by finite-source effects (Bennett & Rhie 1996). In computing finite-source magnifications, we consider the limb-darkening variation of the source.

One also needs extra parameters to describe the lensing light curve of a 1L2S event. These parameters are $(t_{0,2}, u_{0,2}, q_F)$, which represent the closest approach time and separation between the lens and the second source, and the flux ratio between the binary source stars, respectively. In the 1L2S model, we designated the lensing parameters related to the primary source, S_1, so as $(t_{0,1}, u_{0,1})$ to distinguish them from those related to the source companion, S_2. In order to consider finite-source effects occurring when the lens passes over either of the source stars, we added two additional parameters of the normalized source radii, ρ_1 and ρ_2, for the lens transits over S_1 and S_2, respectively (Dominik 2019).

In modeling 1L1S and 1L2S light curves, for which the lensing magnification is smooth with the variation of the lensing parameters, we search for the solution of the lensing parameters via a downhill approach by minimizing χ^2 using the Markow chain Monte Carlo (MCMC) algorithm. In modeling 2L1S light curves, for which the lensing magnification variation is discontinuous due to the formation of caustics and there may exist multiple local solutions caused by various types of degeneracy, we model the light curves in two steps. In the first step, we conduct grid searches for the binary parameters s and q, construct a χ^2 map on the s–q parameter plane, and we then identify local solutions appearing on the χ^2 map. In the second step, we polish the individual local solutions using the downhill approach. Below we present the details of the modeling conducted for the individual lensing events.

3.1. OGLE-2017-BLG-1691 (KMT-2017-BLG-0752)

The lensing event OGLE-2017-BLG-1691 occurred during the 2017 bulge season. It was first found by the OGLE survey, and later confirmed by the KMTNet survey from the post-season analyses of the data collected during the season. The KMTNet group designated the event as KMT-2017-BLG-0752. Hereafter, we use the nomenclatures of events by the ID references of the surveys who first found the events in accordance with the convention of the microlensing community. The baseline magnitude of the event was $I_{\rm base} = 19.900 \pm 0.004$.

The lensing light curve of OGLE-2017-BLG-1691 is shown in Fig. 2, where the bottom panel shows the whole view and the top panel displays the enlargement of the region around the anomaly. The event was alerted by the OGLE survey on 2017 September 6, HJD′ ≡ HJD − 2 450 000 ∼ 8002.5, which approximately corresponds to the time near the peak. An anomaly occurred about one day after the peak, but it was not noticed during the progress of the event because it was covered by

Table 3. Lensing parameters of OGLE-2017-BLG-1691.

Parameter	2L1S (Inner)	2L1S (Outer)	1L2S
χ^2	866.9	866.5	880.4
t_0 (HJD′)	8002.540 ± 0.010	8002.531 ± 0.010	8002.499 ± 0.012
u_0 (10^{-2})	4.83 ± 0.27	4.95 ± 0.26	6.55 ± 0.49
t_E (days)	19.42 ± 0.83	18.94 ± 0.82	18.77 ± 0.83
s	1.058 ± 0.011	1.003 ± 0.014	–
q (10^{-4})	0.708 ± 0.23	0.97 ± 0.34	–
α (rad)	3.873 ± 0.012	3.865 ± 0.010	–
ρ (10^{-3})	3.40 ± 0.47	3.54 ± 0.52	–
$t_{0,2}$ (HJD′)	–	–	8003.587 ± 0.015
$u_{0,2}$ (10^{-2})	–	–	0.029 ± 0.124
ρ_2 (10^{-3})	–	–	3.39 ± 0.93
q_F (10^{-3})	–	–	6.11 ± 1.85

Notes. HJD′ = HJD − 2 450 000.

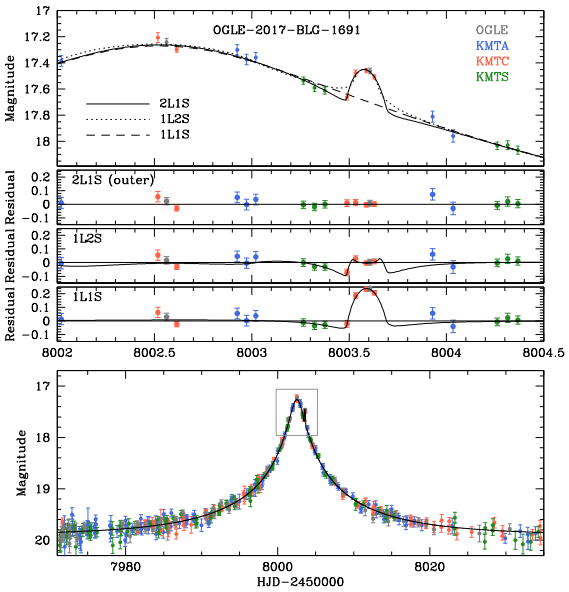

Fig. 2. Lensing light curve of OGLE-2017-BLG-1691. *Bottom panel*: whole view, and the *top panel* displays the enlargement of the region around the anomaly (the region enclosed by a box in the bottom panel). In the *top panel*, curves of the three tested models, 2L1S (outer), 1L2S, and 1L1S models, are drawn over the data points, and the residuals from the individual models are presented in the three *middle panels*. The curve drawn in the bottom panel is the best-fit model (outer 2L1S model). Colors of data points are set to match those of the telescopes used for observations marked in the legend. The curves drawn in the 1L2S and 1L1S residual panels represent the differences from the 2L1S model.

just a single OGLE data point and the KMTNet data were not released during the lensing magnification. The existence of the anomaly was identified five years after the event, shortly after the re-reduction of all 2017 KMT light curves, from a project of reinvestigating the previous KMTNet data conducted to find unnoticed planetary signals (Han et al. 2022b). The top panel of Fig. 2 shows that the anomaly, which lasted for ∼5 h centered at HJD′ ∼ 8003.6, was additionally covered by three KMTC data points, and this confirmed that the single anomalous OGLE point was real.

We model the light curve of the event under the 1L1S, 2L1S, and 1L2S interpretations. The residuals of the individual tested models are compared in Fig. 2. It is found that the 2L1S model best describes the anomaly, being favored over the 1L1S and 1L2S models by $\Delta\chi^2 = 456.1$ and 13.9, respectively. From the comparison of the residuals, it is found that the 2L1S model is confirmed not only by the 4 data points (3 KMTC plus 1 OGLE points) with positive deviations near the peak of the bump but also by the three additional points (2 KMTS and 1 KMTC points) before the major bump with slightly negative deviations.

We find two degenerate 2L1S solutions with binary parameters of $(s, q) \sim (1.058, 0.71 \times 10^{-4})$ and $\sim (1.003, 0.97 \times 10^{-4})$, which we designate as "inner" and "outer" solutions, respectively, for the reason to be mentioned below. We list the full lensing parameters of the two 2L1S solutions in Table 3, together with the parameters of the 1L2S model. The degeneracy is very severe and the outer solution is favored only by $\Delta\chi^2 = 0.4$. The lensing parameters of the solutions indicate that the anomaly was produced by a very small mass-ratio planetary companion to the lens lying close to the Einstein ring of the primary regardless of the solutions. From the fact that both solutions have separations greater than unity and do not follow the relation of $s_{\rm inner} \times s_{\rm outer} \simeq 1$, the degeneracy is different from the "close-wide" degeneracy (Griest & Safizadeh 1998; Dominik 1999; An 2005), which arises due to the similarity between the central caustics of planetary lens systems with planet separations s and $1/s$. Instead, the planet separations of the two degenerate solutions follow the relation:

$$\sqrt{s_{\rm in} \times s_{\rm out}} = s^{\dagger}; \qquad s^{\dagger} = \frac{\sqrt{u_{\rm anom}^2 + 4} + u_{\rm anom}}{2}, \tag{1}$$

where $u_{\rm anom}^2 = \tau_{\rm anom}^2 + u_0^2$, $\tau_{\rm anom} = (t_{\rm anom} - t_0)/t_{\rm E}$, and $t_{\rm anom}$ indicates the time of the planetary anomaly (Hwang et al. 2022; Zhang et al. 2022; Ryu et al., in prep.). With the values $t_0 \simeq 8002.5$, $u_0 \simeq 4.85 \times 10^{-2}$, $t_{\rm E} \simeq 19$ day, and $t_{\rm anom} \simeq 8003.6$, one finds that $s^{\dagger} \simeq 1.04$, which matches well $\sqrt{s_{\rm in} \times s_{\rm out}} \simeq 1.03$. This indicates that the similarity between the light curves of the two solutions is caused by the degeneracy identified by Yee et al. (2021), who first mentioned the continuous transition between the "close-wide" and "inner-outer" (Gaudi & Gould 1997) degeneracies. Hereafter, we refer to this degeneracy as "offset degeneracy" following Zhang et al. (2022).

Figure 3 shows the lens systems configurations, in which the source trajectory (line with an arrow) with respect to the caustic and positions of the lens components (blue solid dots

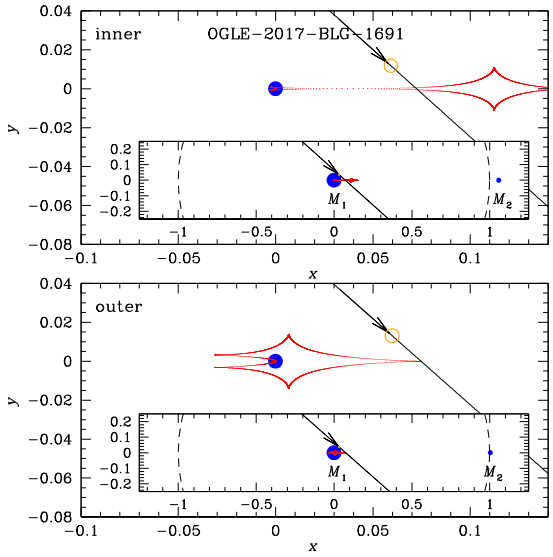

Fig. 3. Lens system configurations of OGLE-2017-BLG-1691: *upper panel* (inner solution) and *lower panel* (outer solution). The inset in each panel shows the whole view of the lens system, and the main panel presents the zoom-in view of the caustics. The red cuspy figure is the caustic and the line with an arrow is the source trajectory. The orange circle on the trajectory is drawn to represent the source scale with respect to the caustic. The blue solid dots marked by M_1 and M_2 indicate the positions of the host and planet, respectively. The dashed circle with unit radius in the inset represents the Einstein ring.

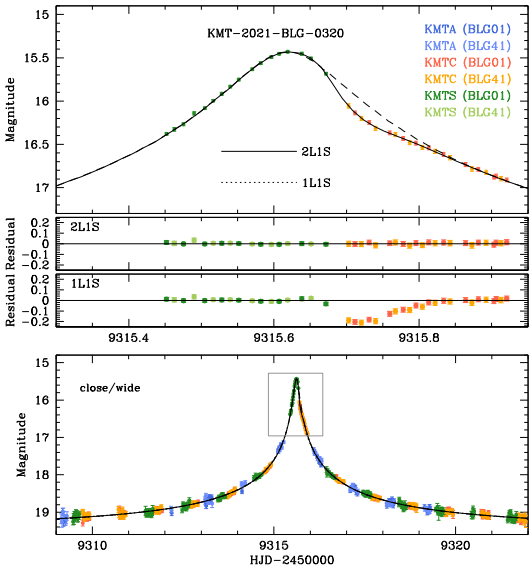

Fig. 4. Lensing light curve of KMT-2021-BLG-0320. Notations are the same as those in Fig. 2.

Table 4. Lensing parameters of KMT-2021-BLG-0320.

Parameter	Close	Wide
χ^2	4075.5	4075.5
t_0 (HJD′)	9315.615 ± 0.001	9315.615 ± 0.001
u_0 (10^{-3})	5.86 ± 0.21	5.93 ± 0.21
t_E (days)	13.12 ± 0.39	12.97 ± 0.40
s	0.771 ± 0.014	1.274 ± 0.024
q (10^{-4})	3.02 ± 0.42	2.89 ± 0.44
α (rad)	0.604 ± 0.014	0.602 ± 0.014
ρ (10^{-3})	–	–

marked by M_1 and M_2) is presented: inner solution in the upper panel and outer solution in the lower panel. The source passed the inner side (with respect to M_1) of the caustic according to the inner solution, while the source passes the outer side according to the outer solution. For both solutions, the source crossed the cusp of the caustic and thus the anomaly is affected by finite-source effects during the caustic crossing, allowing us to precisely measure the normalized source radius. For each solution, the source size relative to the caustic is represented by an orange circle marked on the source trajectory. As discussed in Sect. 4, the measurement of ρ is important to estimate the lensing observable of the angular Einstein radius θ_E, which can be used to constrain the physical lens parameters. However, the microlens parallax vector, $\pi_E = (\pi_{rel}/\theta_E)/(\boldsymbol{\mu}/\mu)$, which is another observable constraining the physical lens parameters, cannot be securely measured because the event time scale, $t_E \sim 19$ days, is not long enough to produce detectable deviations induced by the orbital motion of Earth around the Sun (Gould 1992). Here, $\boldsymbol{\mu}$ represents the vector of the relative lens-source proper motion.

3.2. KMT-2021-BLG-0320

The lensing event KMT-2021-BLG-0320 was found on 2021 April 9 (HJD′ ∼ 9313) when the event had not yet reached its peak, with the employment of the KMTNet AlertFinder system (Kim et al. 2018), which had been in full operation since the 2019 season. Two days after the detection, the event reached its peak with a magnification of $A_{max} \sim 170$, and then gradually declined until it reached its baseline of $I_{base} = 20.08$. The source of the event lies in the two KMTNet prime fields of BLG01 and BLG41, toward which observations were conducted with a 30 min cadence for each field, and thus with a 15 min combined cadence. The areas covered by the two fields overlap except for about 15% of the area of each field filling the gaps between the chips of the camera. Because the data were taken from two fields of three telescopes, there are 6 data sets: KMTA (BLG01), KMTA (BLG41), KMTC (BLG01), KMT (BLG41), KMTS (BLG01), and KMTS (BLG41).

In Fig. 4, we present the light curve constructed from the combination of the 6 KMTNet data sets. Although it would be difficult to notice the anomaly from a glimpse, we inspected the light curve because the event reached a very high magnification at the peak, near to which the light curve is susceptible to perturbations induced by a planet (Griest & Safizadeh 1998). From this inspection, it was found that the light curve exhibited an anomaly that lasted for about 4 h with a negative deviation with respect to a 1L1S model. We refer to the enlarged view around the peak region of the light curve presented in the top panel of Fig. 4. It is known that a planetary companion to a lens can induce anomalies with both positive and negative deviations, while a faint companion to a source can induce anomalies with only positive deviations (Gaudi 1998). We therefore modeled the light curve under the 2L1S interpretation.

It has been found that the anomaly is well described by a 2L1S model, in which the mass ratio between the binary lens components is very low. We found two sets of solutions with $(s, q)_{close} \sim (0.77, 3.0 \times 10^{-4})$ and $(s, q)_{wide} \sim (1.27, 2.9 \times 10^{-4})$. We designate the individual solutions as "close" and "wide" solutions because the former solution has $s < 1.0$ and the latter has $s > 1.0$. In Table 4, we list the full lensing parameters for the two sets of solutions. The fits of the two solutions are

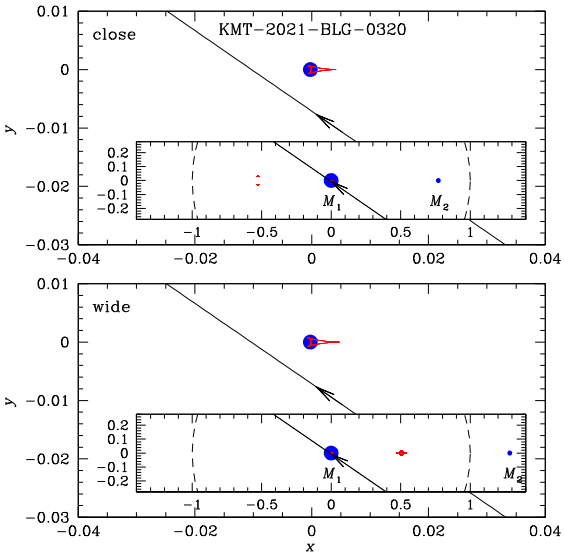

Fig. 5. Lens system configurations of KMT-2021-BLG-0320. *Upper and lower panels*: configurations of the close and wide solutions, respectively.

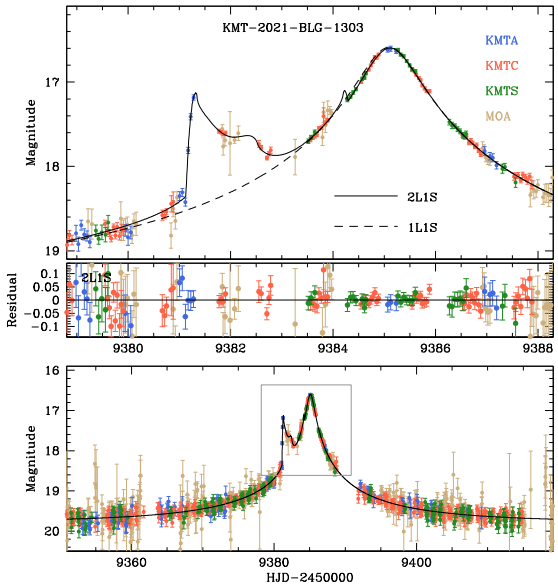

Fig. 6. Lensing light curve of KMT-2021-BLG-1303. Notations are the same as those in Fig. 2.

nearly identical with χ^2 values that are equal to the first digit after the decimal point, indicating that the degeneracy between the two solutions is very severe. The fact that the binary separations of the two solutions follow the relation of $s_{\rm close} \times s_{\rm wide} \simeq 1.0$ indicates that the similarity between the solution stems from the close-wide degeneracy. It is known that the relation between the planet separations of the solutions under the offset degeneracy in Eq. (1) applies to more general cases (including the resonant case) than the $s_{\rm close} \times s_{\rm wide} \simeq 1.0$ relation of the close-wide degeneracy, and we confirm this. In addition to the relation between $s_{\rm in}$ and $s_{\rm out}$, Hwang et al. (2022) provided analytic formulas for the heuristic estimation of the source trajectory angle and the mass ratio;

$$\alpha = \tan^{-1}\left(\frac{u_0}{\tau_{\rm anom}}\right); \qquad q = \left(\frac{\Delta t_{\rm anom}}{4t_{\rm E}}\right)\left(\frac{s}{|u_0|}\right)\left|\sin^3\alpha\right|, \tag{2}$$

where $\Delta t_{\rm anom}$ denotes the duration of the planet-induced anomaly. We confirm that the heuristically estimated values of α and q match well those estimated from the modeling. It was found that the normalized source radius could not be constrained, not even the upper limit, and thus the line for ρ in Table 4 is left blank.

Figure 5 shows the lensing configuration of KMT-2021-BLG-0320 for the close (upper panel) and wide (lower panel) solutions. It shows that the source passed the back-end region of the tiny central caustic induced by a planet, and this generated the negative deviation of the observed anomaly. The central caustics of the close and wide solutions are very similar, resulting in nearly identical deviations. Because the source passed well outside the caustic, finite-source effects could not be detected and, thus, we do not mark an orange circle representing the source size. Microlens-parallax effects could not be securely detected because the event time scale, $t_{\rm E} \sim 13$ days, is much shorter than the orbital period of Earth, namely, one year.

3.3. KMT-2021-BLG-1303 (MOA-2021-BLG-182)

The event KMT-2021-BLG-1303 was first found on 2021 June 14 (HJD′ ∼ 9379) by the KMTNet survey, and later identified by the MOA survey on 2021 June 17 (HJD′ ∼ 9382). The MOA survey designated the event as MOA-2021-BLG-182. A day after the first discovery, the event displayed an anomaly that lasted for about 2 days. After the anomaly, the event reached peak at HJD′ ∼ 9385.1 with a magnification of $A_{\rm max} \sim 46$, and then gradually declined to the baseline of $I_{\rm base} = 19.67$.

Table 5. Lensing parameters of KMT-2021-BLG-1303.

Parameter	Value
χ^2	1654.9
t_0 (HJD′)	9385.091 ± 0.003
u_0 (10^{-2})	2.17 ± 0.06
$t_{\rm E}$ (days)	25.21 ± 0.68
s	1.029 ± 0.001
q (10^{-4})	6.42 ± 0.45
α (rad)	6.138 ± 0.001
ρ (10^{-3})	0.95 ± 0.08

The light curve of KMT-2021-BLG-1303 constructed with the combined KMTNet and MOA data is shown in Fig. 6. Compared to the previous two events, the light curve of this event displays a very obvious anomaly with a maximum deviation of $\Delta I \sim 1.4$ mag from a 1L1S model. The rapid brightening at HJD′ ∼ 9381.0 indicates that the event experienced a caustic crossing. Since caustics form due to the multiplicity of lens components, we ruled out the 1L2S origin of the anomaly and tested only the 2L1S interpretation.

We find that the anomaly is well explained by a 2L1S model with a planetary companion lying close to the Einstein ring of the host. We found a unique solution without any degeneracy, and the binary parameters of the solution are $(s, q) \sim (1.029, 6.4 \times 10^{-4})$. Here, the planet-to-host mass ratio is on the order of 10^{-4}, as in the two previous events. We double checked the uniqueness of the solution by thoroughly inspecting the region around the s and q parameters predicted by the relations in Eqs. (1) and (2), and confirmed that there is only a single solution. The full lensing parameters of the event are listed in Table 5.

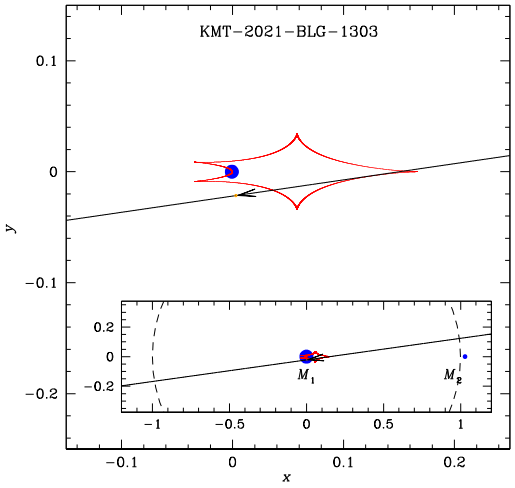

Fig. 7. Lens system configuration of KMT-2021-BLG-1303. Notations are the same as those in Fig. 3.

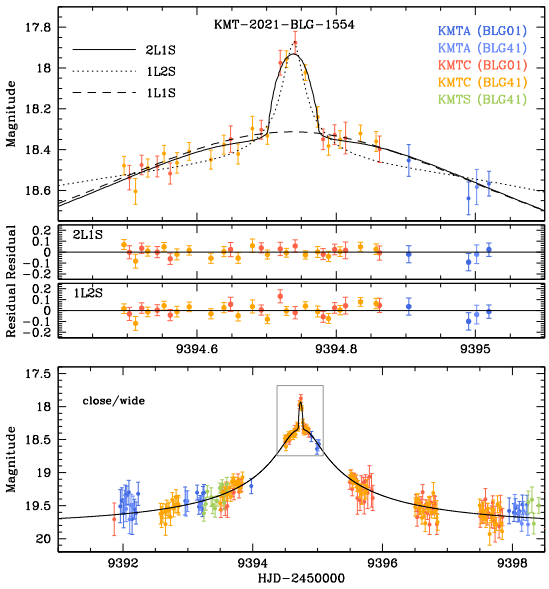

Fig. 8. Lensing light curve of KMT-2021-BLG-1554. Notations are the same as those in Fig. 2.

The lensing configuration of the event is presented in Fig. 7, which shows that the planet lies very close to the Einstein ring and induces a single six-sided resonant caustic near the primary of the lens. The source entered the caustic at HJD′ ∼ 9381.0, and this produced the sharp rise of the light curve at the corresponding time. According to the model, the source exited the caustic at HJD′ ∼ 9384.2, but the caustic-crossing feature at this epoch is not obvious in the lensing light curve due to the combination of the weak caustic and the poor coverage of the region. The pattern of the anomaly between the caustic entrance and exit deviates from a typical "U"-shape pattern because the source passed along the fold of the caustic. The light curve during the caustic entrance of the source was well resolved by the KMTA data, and thus the normalized source radius, $\rho = (0.95 \pm 0.08) \times 10^{-3}$, is tightly constrained. However, it was difficult to constrain the microlens parallax because the time scale, $t_{\rm E} \sim 25$ days, is not long enough and the photometric precision of the faint source with $I \sim 21$ is not high enough to detect subtle deviations induced by microlens-parallax effects.

3.4. KMT-2021-BLG-1554

This short event with a time scale of $t_{\rm E} \sim 5$ days and a faint baseline magnitude of $I_{\rm base} = 22.39$ was detected on 2021 Jul. 1 (HJD′ ∼ 9396), about two days after the event peaked at $t_0 \sim$ 9394.7, by the KMTNet survey. The source lies in the prime fields of BLG01 and BLG41 and, thus, there are six data sets from the three KMTNet telescopes. Among these data sets, the data set of the BLG41 field acquired by the KMTS telescope was not used in the analysis due to its poor photometric quality caused by bad seeing during the lensing magnification. Although the other data set from KMTS and those from KMTA were included in the analysis, the results are mainly derived from the KMTC data sets, which cover the peak region of the light curve.

The light curve constructed with the available KMTNet data sets is shown in Fig. 8. In the peak region, it exhibits an anomaly that lasted for about three hours from a 1L1S model with a positive deviation of $\Delta I \sim 0.5$ mag. The anomaly appears both in the BLG01 (two data points) and BLG41 (3 points) data sets obtained from KMTC observations, confirming that the signal is real. Because a positive anomaly can be produced by a binary companion to either a lens or a source, we test both 2L1S and 1L2S models.

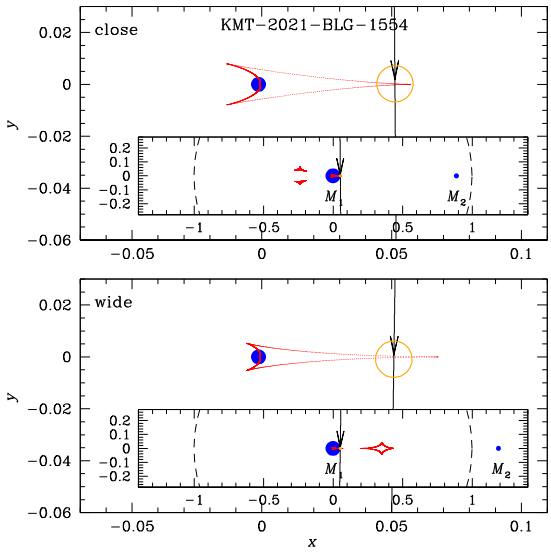

Fig. 9. Lens system configuration of KMT-2021-BLG-1554. Notations are the same as those in Fig. 5.

Detailed analysis of the light curve indicates that the anomaly was produced by a planetary companion to the lens. We find two sets of solutions with planet parameters of $(s, q)_{\rm close} \sim (0.89, 1.4 \times 10^{-3})$ and $(s, q)_{\rm wide} \sim (1.12, 1.5 \times 10^{-3})$ resulting from the close-wide degeneracy. The full lensing parameters of both solutions are provided in Table 6. It is found that the degeneracy between the two 2L1S solution is severe with $\Delta\chi^2 = 0.3$, and the 2L1S solutions are favored over the model under the 1L2S interpretation by $\Delta\chi^2 \sim 11$. The lensing parameters of the 1L2S model are listed in Table 6. We compare the residuals of the 2L1S and 1L2S models in the two middle panels of Fig. 8. It appears that the source crossed a caustic and thus we are able to measure the normalized source radius, $\rho = (6.98 \pm 1.18) \times 10^{-3}$.

The lensing configurations of the event according to the close and wide solutions are shown in the upper and lower panels of Fig. 9, respectively. The figure shows that the anomaly was produced by the crossing of the source over the sharp tip of the

Table 6. Lensing parameters of KMT-2021-BLG-1554.

Parameter	2L1S (Close)	2L1S (Wide)	1L2S
χ^2	3486.0	3485.7	3496.1
t_0 (HJD′)	9394.737 ± 0.010	9394.742 ± 0.010	9394.719 ± 0.019
u_0	0.051 ± 0.009	0.051 ± 0.011	0.003 ± 0.054
t_E (days)	5.04 ± 0.78	5.15 ± 0.72	6.55 ± 1.11
s	0.888 ± 0.039	1.189 ± 0.051	–
q (10^{-4})	14.14 ± 4.48	14.94 ± 5.41	–
α (rad)	4.705 ± 0.038	4.727 ± 0.037	–
ρ (10^{-3})	6.98 ± 1.18	7.00 ± 1.28	98.8 ± 24.2
$t_{0,2}$ (HJD′)	–	–	9394.740 ± 0.002
$u_{0,2}$	–	–	0.002 ± 0.002
ρ_2 (10^{-3})	–	–	–
q_F	–	–	0.048 ± 0.008

central caustic induced by a planet lying near the Einstein ring of the planet host. The gap between the caustic entrance and exit is much smaller than the source size, and thus the individual caustic-crossing features do not show up in the anomaly and instead the anomaly appears as a single bump. The incidence angle of the source on the binary axis is nearly 90° and thus the features on the rising and falling sides of the anomaly are symmetric.

4. Source stars and angular Einstein radii

Among the four analyzed planetary events, the anomalies of the three events (KMT-2017-BLG-0752, KMT-2021-BLG-1303, and KMT-2021-BLG-1554) were affected by finite-source effects, and thus the normalized source radii can be measured. In this section, we estimate the angular Einstein radii for these events. Estimating θ_E from a measured ρ value requires us to specify the source type, from which the angular source radius θ_* is deduced and the Einstein radius is determined by:

$$\theta_E = \frac{\theta_*}{\rho}. \quad (3)$$

Although the normalized source radius and thus θ_E cannot be measured for the event KMT-2021-BLG-0320, we specify the source type for the sake of completeness.

The specification of the source type is done by estimating the color and brightness of the source. We measure the I and V-band magnitudes of the source from the regression of the data processed using the pyDIA photometry code (Albrow 2017) with the variation of the lensing magnification. We then place the source on the instrumental color-magnitude diagram (CMD) of stars lying around the source constructed using the same photometry code. Following the method of Yoo et al. (2004), the instrumental source color and magnitude, $(V-I, I)$ are then calibrated using the centroid of red giant clump (RGC), for which its reddening and extinction-corrected (de-reddened) color and magnitude, $(V-I, I)_{RGC,0}$, are known, on the CMD as a reference.

Figure 10 shows the positions of the source stars (marked by blue dots) with respect to those of the RGC centroids (red dots) on the CMDs of the individual events. For OGLE-2017-BLG-1691, the source color could not be securely measured not only because the V-band data sparsely covered the light curve during the lensing magnification but also because the photometry

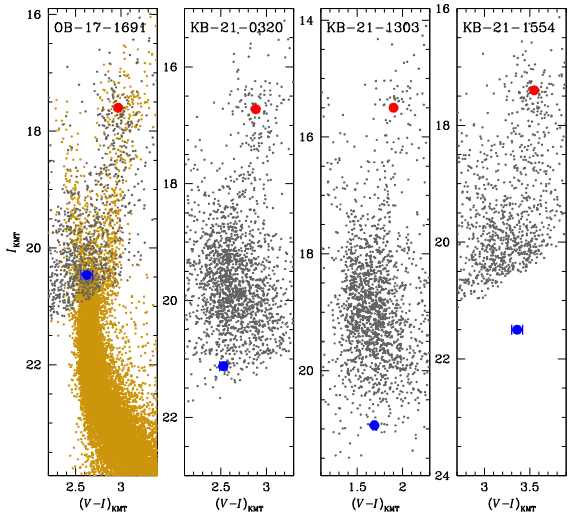

Fig. 10. Source locations with respect to the centroids of the red giant clump (RGC) on the instrumental color-magnitude diagrams of stars lying around the source stars of the events OGLE-2017-BLG-1691, KMT-2021-BLG-0320, KMT-2021-BLG-1303, and KMT-2021-BLG-1554. For OGLE-2017-BLG-1691, the CMD is constructed by combining the two CMDs from KMTC (grey dots) and HST (brown dots) observations. For each event, the locations of the source and RGC centroid are marked by blue and red solid dots, respectively.

quality of these data is low, although the I-band magnitude was relatively well measured. In this case, we estimated the source color as the median color of stars with the same I-band magnitude offset from the RGC centroid in the CMD constructed from the images of Baade's window taken from the observations using the *Hubble* Space Telescope (Holtzman et al. 1998). From the offsets in color and magnitudes between the source and RGC centroid, $\Delta(V-I, I)$, together with the known de-reddened color and magnitude of the RGC centroid, $(V-I, I)_{RGC,0}$ (Bensby et al. 2013; Nataf et al. 2013), we estimate the calibrated source color and magnitude as $(V-I, I)_0 = (V-I, I)_{RGC,0} + \Delta(V-I, I)$. In Table 7, we list the source colors and magnitudes of the individual events estimated from this procedure along with the spectral types of the source stars. It has been found that the source of OGLE-2017-BLG-1691 is a turnoff star or a subgiant of a G spectral type, while the source stars of the other events are main-sequence stars with spectral types ranging from G to K.

Table 7. De-reddened colors, magnitudes, and spectral types of source stars.

Event	$(V-I)_0$	I_0	Spectral type
OGLE-2017-BLG-1691	0.714 ± 0.065	17.397 ± 0.039	G1 turnoff or subgiant
KMT-2021-BLG-0320	0.700 ± 0.040	18.843 ± 0.002	G1V
KMT-2021-BLG-1303	0.849 ± 0.015	19.809 ± 0.003	G9V
KMT-2021-BLG-1554	0.873 ± 0.061	18.649 ± 0.008	K1V

Table 8. Angular source radii, Einstein radii, and relative lens-source proper motions.

Event	θ_* (μas)	θ_E (mas)	μ (mas yr^{-1})
OGLE-2017-BLG-1691	1.043 ± 0.100	0.30 ± 0.05	5.68 ± 1.01
KMT-2021-BLG-0320	0.528 ± 0.042	–	–
KMT-2021-BLG-1303	0.401 ± 0.029	0.42 ± 0.05	6.13 ± 0.70
KMT-2021-BLG-1554	0.703 ± 0.065	0.10 ± 0.02	7.30 ± 1.50

For each event, the angular source radius and Einstein radius were estimated from the measured color and magnitude of the source. For this, the measured $V-I$ color was converted into $V-K$ color using the color-color relation of Bessell & Brett (1988), θ_* value was interpolated from the $(V-K)$–θ_* relation of Kervella et al. (2004), and then the angular Einstein radius was estimated using the relation in Eq. (3). With the measured Einstein radius together with the event time scale, the value of the relative lens-source proper motion was assessed as

$$\mu = \frac{\theta_E}{t_E}. \tag{4}$$

In Table 8, we list the estimated values of θ_*, θ_E, and μ for the individual events. The θ_E and μ values for the event KMT-2021-BLG-0320 are left blank because finite-source effects in the lensing light curve were not detected and subsequently the values of ρ, θ_E, and μ could not be measured. We note that the angular Einstein radius of KMT-2021-BLG-1554, $\theta_E \sim 0.10$ mas, is substantially smaller than those of the other events, and this together with its short time scale, $t_E \sim 5$ days, suggests that the mass of the lens would be very low. KMT-2021-BLG-1554 is the seventh shortest microlensing event with a bound planet. For details, we refer to Table 3 of Ryu et al. (2021).

5. Physical parameters

In this section, we estimate the physical parameters of the planetary systems. For the unique constraint of the physical lens parameters, it is necessary to simultaneously measure the extra observables of θ_E and π_E, from which the mass M and distance to the lens, D_L, are determined as:

$$M = \frac{\theta_E}{\kappa \pi_E}; \qquad D_L = \frac{\mathrm{AU}}{\pi_E \theta_E + \pi_S}. \tag{5}$$

Here, $\kappa = 4G/(c^2\mathrm{AU})$, $\pi_S = \mathrm{AU}/D_S$, and D_S denotes the distance to the source (Gould 1992, 2000). The values of the microlens parallax could not be measured for any of the events, and thus the physical parameters cannot be unambiguously determined from the relation in Eq. (5). However, one can still constrain M and D_L using the other measured observables of t_E and θ_E, which are related to the physical lens parameters as

$$t_E = \frac{\theta_E}{\mu}; \qquad \theta_E = (\kappa M \pi_{rel})^{1/2}, \tag{6}$$

where $\pi_{rel} = \mathrm{AU}(D_L^{-1} - D_S^{-1})$ denotes the relative parallax between the lens and source. The event time scales were well measured for all events, and the Einstein radii were assessed for three of the four events. In order to estimate the physical lens parameters with the constraints provided by the measured observables of the individual events, we conducted Bayesian analyses using a Galactic model.

In the Bayesian analysis, we started by producing many lensing events from a Monte Carlo simulation conducted with the use of a Galactic model, which defines the matter-density and kinetic distributions, and mass function of Galactic objects. We adopted the Galactic model constructed by Jung et al. (2021). In this model, the density distributions of disk and bulge objects are described by the Robin et al. (2003) and Han & Gould (2003) models, respectively. The kinematic distribution of disk objects is based on the modified version of the Han & Gould (1995) model, in which the original version is modified to reconcile the changed density model, that is, the Robin et al. (2003) model. The bulge kinematic distribution is modeled based on proper motions of stars in the *Gaia* catalog (Gaia Collaboration 2016, 2018). For the details of the density and kinematic distributions, we refer to Jung et al. (2021). In the Galactic model, the mass function is constructed with the adoption of the initial mass function and the present-day mass function of Chabrier (2003) for the bulge and disk lens populations, respectively.

In the second step, we computed the time scales and Einstein radii of the simulated events using the relations in Eq. (6), and then constructed posterior distributions of M and D_L for the simulated events with the t_E and θ_E values that are consistent with the observables of the individual lensing events. For the three events OGLE-2017-BLG-1691, KMT-2021-BLG-1303, and KMT-2021-BLG-1554, we use the constraints of both t_E and θ_E, and for KMT-2021-BLG-0320, we only apply the constraint for t_E because θ_E is not measured for the event.

Figures 11 and 12 show the Bayesian posteriors of M and D_L of the individual events, respectively. In Table 9, we summarize the estimated values of the host and planet masses, M_{host} and M_{planet}, distance, and projected host-planet separation,

Table 9. Physical lens parameters.

Event	$M_{\rm host}$ ($M_\odot$)	$M_{\rm planet}$ ($M_{\rm J}$)	$D_{\rm L}$ (kpc)	$a_\perp$ (AU)
OGLE-2017-BLG-1691	$0.45^{+0.36}_{-0.25}$	$0.046^{+0.037}_{-0.025}$	$7.29^{+1.01}_{-1.33}$	$2.41^{+0.34}_{-0.44}$ (inner)
	–	–	–	$2.54^{+0.36}_{-0.46}$ (outer)
KMT-2021-BLG-0320	$0.32^{+0.39}_{-0.21}$	$0.10^{+0.13}_{-0.07}$	$6.95^{+1.07}_{-1.33}$	$1.54^{+0.24}_{-0.30}$ (close)
	–	–	–	$2.55^{+0.39}_{-0.49}$ (wide)
KMT-2021-BLG-1303	$0.57^{+0.32}_{-0.29}$	$0.38^{+0.22}_{-0.20}$	$6.28^{+0.95}_{-1.43}$	$2.89^{+0.44}_{-0.66}$
KMT-2021-BLG-1554	$0.08^{+0.13}_{-0.04}$	$0.12^{+0.20}_{-0.07}$	$7.68^{+1.04}_{-1.10}$	$0.72^{+0.13}_{-0.14}$ (close)
	–	–	–	$0.96^{+0.15}_{-0.16}$ (wide)

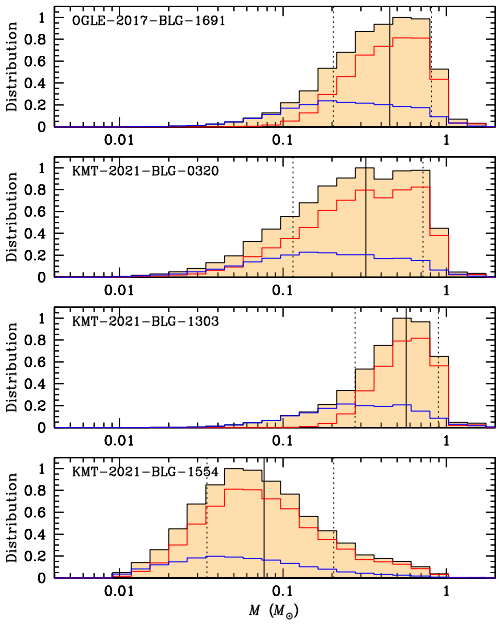

Fig. 11. Bayesian posteriors of the host masses of the planetary systems. For each distribution, the solid vertical line indicates the median value, and the dotted lines represent 1σ range of the distribution. The blue and red curves represent the distributions contributed by disk and bulge populations of lenses, respectively, and the black curve is the sum from the two lens populations.

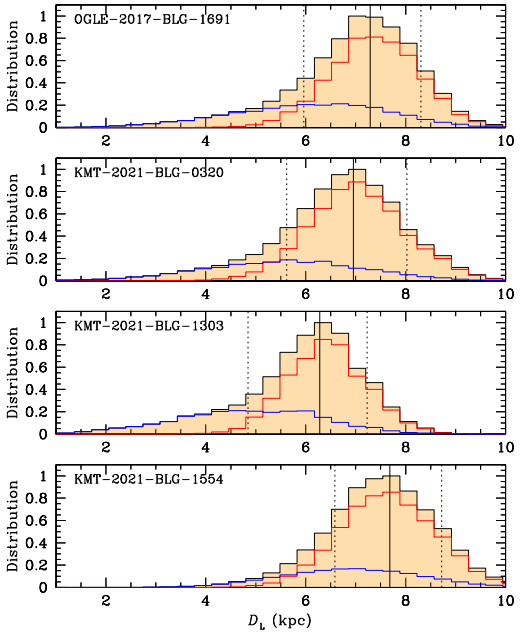

Fig. 12. Bayesian posteriors of the distances to the planetary systems. Notations are the same as those in Fig. 11.

$a_\perp = sD_{\rm L}\theta_{\rm E}$, for all of which medians are presented as representative values and the uncertainties are estimated as 16% and 84% of the Bayesian posterior distributions. The median values and uncertainty ranges of the individual events are marked by solid and dotted vertical lines in the Bayesian posteriors presented in Figs. 11 and 12, respectively. For the events with degenerate solutions, OGLE-2017-BLG-1691, KMT-2021-BLG-0320, and KMT-2021-BLG-1554, we present the planetary separations $a_\perp$ corresponding to both the close and wide (or inner and outer) solutions. We note that the uncertainties of the estimated physical parameters are big because of the intrinsically weak Bayesian constraint. For example, from the comparison of the posterior distributions of OGLE-2017-BLG-1691 and KMT-2021-BLG-0320, one finds that the difference between the two posterior distributions is not significant, although the mean lens mass for the former event is slightly bigger than that of the latter event due to the longer time scale and the uncertainty is smaller due to the additional constraint of $\theta_{\rm E}$.

The estimated masses indicate that all of the discovered planets have sub-Jovian masses. The planet masses of KMT-2021-BLG-0320L, KMT-2021-BLG-1303L, and KMT-2021-BLG-1554L correspond to ~0.10, ~0.38, and ~0.12 times the mass of the Jupiter, and the planet mass of OGLE-2017-BLG-1691L corresponds to that of Uranus. To be noted among the planet hosts is that the estimated mass of the planetary system KMT-2021-BLG-1554L, $M_{\rm host} \sim 0.08\ M_\odot$, corresponds to the boundary between a star and a brown dwarf (BD). Together with the previously detected planetary systems with very low-mass hosts[2], the discovery of the system demonstrates the microlensing capability of detecting planetary systems with very faint or substellar hosts. Besides KMT-2021-BLG-1554L, the host stars of the other planetary systems are low-mass stars with masses

[2] MOA-2011-BLG-262 (Bennett et al. 2014), OGLE-2012-BLG-0358 (Han et al. 2013), MOA-2015-BLG-337 (Miyazaki et al. 2018), OGLE-2015-BLG-1771 (Zhang et al. 2020), KMT-2016-BLG-1820 (Jung et al. 2018a), KMT-2016-BLG-2605 (Ryu et al. 2021), OGLE-2017-BLG-1522 (Jung et al. 2018b), OGLE-2018-BLG-0677 (Herrera-Martín et al. 2020), KMT-2018-BLG-0748 (Han et al. 2020b), and KMT-2019-BLG-1339L (Han et al. 2020a).

lying in the range of ~[0.3–0.6] $M_\odot$. Based on the approximation that the snow line distance scales with the host mass as $a_{\rm sl} \sim 2.7(M/M_\odot)$ AU, all discovered planets lie beyond the snow lines of the hosts regardless of the solutions, demonstrating the high microlensing sensitivity to cold planets. The planetary systems lie in the distance range of ~[6.3–7.6] kpc, demonstrating the usefulness of the microlensing method in detecting remote planets.

6. Summary and conclusion

We presented the analyses of four planetary microlensing events OGLE-2017-BLG-1691, KMT-2021-BLG-0320, KMT-2021-BLG-1303, and KMT-2021-BLG-1554. The events share a common characteristic that the planetary signals appeared as anomalies with very short durations, ranging from a few hours to a couple of days, and they were clearly detected solely by the combined data of the high-cadence lensing surveys without additional data from followup observations.

From the detailed analyses of the events, it was found that the signals were generated by planets with low planet-to-host mass ratios: three of the planetary systems with mass ratios on the order of 10^{-4} and the other with a mass ratio slightly greater than 10^{-3}. In the histogram of microlensing planets presented in Fig. 1, we mark the positions of the four planets discovered in this work. The estimated masses indicate that all discovered planets have sub-Jovian masses, in which the planet masses of KMT-2021-BLG-0320Lb, KMT-2021-BLG-1303Lb, and KMT-2021-BLG-1554Lb correspond to ~0.10, ~0.38, and ~0.12 times the mass of the Jupiter, and the mass of OGLE-2017-BLG-1691Lb corresponds to that of Uranus. It has been found that the host of the planetary system KMT-2021-BLG-1554L has a mass that is close to the boundary between a star and a brown dwarf. Besides this system, it has been found that the host stars of the other planetary systems are low-mass stars with masses in the range of ~[0.3–0.6] $M_\odot$. The discoveries of these planets fully demonstrate the capability of the current high-cadence microlensing surveys in detecting low-mass planets.

Acknowledgements. Work by C.H. was supported by the grants of National Research Foundation of Korea (2020R1A4A2002885 and 2019R1A2C2085965). This research has made use of the KMTNet system operated by the Korea Astronomy and Space Science Institute (KASI) and the data were obtained at three host sites of CTIO in Chile, SAAO in South Africa, and SSO in Australia. The OGLE project has received funding from the National Science Centre, Poland, grant MAESTRO 2014/14/A/ST9/00121 to AU. he MOA project is supported by JSPS KAKENHI grant Nos. JSPS24253004, JSPS26247023, JSPS23340064, JSPS15H00781, JP16H06287, JP17H02871, and JP19KK0082.

References

Alard, C., & Lupton, R. H. 1998, ApJ, 503, 325
Albrow, M. 2017, https://doi.org/10.5281/zenodo.268049
Albrow, M., Horne, K., Bramich, D. M., et al. 2009, MNRAS, 397, 2099
An, J. H. 2005, MNRAS, 356, 1409
Bennett, D. P., & Rhie, S. H. 1996, ApJ, 472, 660
Bennett, D. P., Batista, V., Bond, I. A., et al. 2014, ApJ, 785, 155
Bensby, T., Yee, J. C., Feltzing, S., et al. 2013, A&A, 549, A147
Bessell, M. S., & Brett, J. M. 1988, PASP, 100, 1134
Bond, I. A., Abe, F., Dodd, R. J., et al. 2001, MNRAS, 327, 868
Chabrier, G. 2003, PASP, 115, 763
Dominik, M. 1999, A&A, 349, 108
Dominik, M., Bachelet, E., Bozza, V., et al. 2019, MNRAS, 484, 5608
Gaia Collaboration (Prusti, T., et al.) 2016, A&A, 595, A1
Gaia Collaboration (Brown, A. G. A., et al.) 2018, A&A, 616, A1
Gaudi, B. S. 1998, ApJ, 506, 533
Gaudi, B. S., & Gould, A. 1997, ApJ, 486, 85
Gould, A. 1992, ApJ, 392, 442
Gould, A. 2000, ApJ, 542, 785
Gould, A., & Loeb, A. 1992, ApJ, 396, 104
Griest, K., & Safizadeh, N. 1998, ApJ, 500, 37
Han, C., & Gould, A. 1995, ApJ, 447, 53
Han, C., & Gould, A. 2003, ApJ, 592, 172
Han, C., Jung, Y. K., Udalski, A., et al. 2013, ApJ, 778, 38
Han, C., Kim, D., Udalski, A., et al. 2020a, AJ, 160, 64
Han, C., Shin, I.-G., Jung, Y. K., et al. 2020b, A&A, 641, A105
Han, C., Udalski, A., Kim, D., et al. 2021, A&A, 655, A21
Han, C. Bond, I. A., Yee, J. C., et al. 2022a, A&A, 658, A62
Han, C., Gould, A., Albrow, M. D., et al. 2022b, A&A, 658, A94
Han, C., Udalski, A., Lee, C.-U., et al. 2022c, A&A, 658, A93
Herrera-Martín, A., Albrow, A., Udalski, A., et al. 2020, AJ, 159, 134
Holtzman, J. A., Watson, A. M., Baum, W. A., et al. 1998, AJ, 115, 1946
Hwang, K.-H., Zang, W., Gould, A., et al. 2022, AJ, 163, 43
Jung, Y. K., Hwang, K.-H., Ryu, Y.-H., et al. 2018a, AJ, 156, 208
Jung, Y. K., Udalski, A., Gould, A., et al. 2018b, AJ, 155, 219
Jung, Y. K., Han, C., Udalski, A., et al. 2021, AJ, 161, 293
Kervella, P., Thévenin, F., Di Folco, E., & Ségransan, D. 2004, A&A, 426, 29
Kim, S.-L., Lee, C.-U., Park, B.-G., et al. 2016, JKAS, 49, 37
Kim, D.-J., Kim, H.-W., Hwang, K.-H., et al. 2018, AJ, 155, 76
Miyazaki, S., Sumi, T., Bennett, D. P., et al. 2018, AJ, 156, 136
Nataf, D. M., Gould, A., Fouqué, P., et al. 2013, ApJ, 769, 88
Robin, A. C., Reylé, C., Derriére, S., & Picaud, S. 2003, A&A, 409, 523
Ryu, Y. H., Hwang, K.-H., Gould, A., et al. 2021, AJ, 162, 96
Shin, I.-G., Yee, J. C., Hwang K.-H., et al. 2022, AJ, 163, 254
Tomaney, A. B., & Crotts, A. P. S. 1996, AJ, 112, 2872
Udalski, A., Szymański, M. K., & Szymański, G. 2015, Acta Astron., 65, 1
Woźniak, P. R. 2000, Acta Astron., 50, 42
Yee, J. C., Shvartzvald, Y., Gal-Yam, A., et al. 2012, ApJ, 755, 102
Yee, J. C., Zang, W, Udalski, A., et al. 2021, AJ, 162, 180
Yoo, J., DePoy, D. L., Gal-Yam, A., et al. 2004, ApJ, 603, 139
Zang, W., Han, C., Kondo, I., et al. 2021a, Res. Astron. Astroph., 21, 239
Zang, W., Hwang, K.-H., Udalski, A., et al. 2021b, AJ, 162, 163
Zhang, X., Zang, W., Udalski, A., et al. 2020, AJ, 159, 116
Zhang, K., Gaudi, B. S., & Bloom, J. S. 2022, Nature Astronomy, 6, 782

[1] Department of Physics, Chungbuk National University, Cheongju 28644, Republic of Korea
e-mail: cheongho@astroph.chungbuk.ac.kr
[2] Max Planck Institute for Astronomy, Königstuhl 17, 69117 Heidelberg, Germany
[3] Department of Astronomy, The Ohio State University, 140 W. 18th Ave., Columbus, OH 43210, USA
[4] Astronomical Observatory, University of Warsaw, Al. Ujazdowskie 4, 00-478 Warszawa, Poland
[5] Institute of Information and Mathematical Sciences, Massey University, Private Bag 102-904, North Shore Mail Centre, Auckland, New Zealand
[6] Dipartimento di Fisica 'E.R. Caianiello', Universit a di Salerno, Via Giovanni Paolo 132, Fisciano 84084, Italy
[7] Korea Astronomy and Space Science Institute, Daejon 34055, Republic of Korea
[8] University of Canterbury, Department of Physics and Astronomy, Private Bag 4800, Christchurch 8020, New Zealand
[9] Department of Particle Physics and Astrophysics, Weizmann Institute of Science, Rehovot 76100, Israel
[10] Center for Astrophysics, Harvard & Smithsonian 60 Garden St., Cambridge, MA 02138, USA
[11] Department of Astronomy and Tsinghua Centre for Astrophysics, Tsinghua University, Beijing 100084, PR China
[12] School of Space Research, Kyung Hee University, Yongin, Kyeonggi 17104, Republic of Korea
[13] Korea University of Science and Technology, 217 Gajeong-ro, Yuseong-gu, Daejeon, 34113, Republic of Korea
[14] Department of Physics, University of Warwick, Gibbet Hill Road, Coventry, CV4 7AL, UK

[15] Institute for Space-Earth Environmental Research, Nagoya University, Nagoya 464-8601, Japan
[16] Astrophysics Science Division, NASA/Goddard Space Flight Center, Greenbelt, MD20771, USA
[17] Laboratory for Exoplanets and Stellar Astrophysics, NASA, Goddard Space Flight Center, Greenbelt, MD 20771, USA
[18] Department of Astronomy, University of Maryland, College Park, MD 20742, USA
[19] Department of Earth and Planetary Science, Graduate School of Science, The University of Tokyo, 7-3-1 Hongo, Bunkyo-ku, Tokyo, Japan
[20] Instituto de Astrofísica de Canarias, Vía Láctea s/n, E-38205 La Laguna, Tenerife, Spain
[21] Department of Earth and Space Science, Graduate School of Science, Osaka University, 1-1 Machikaneyama, Toyonaka, Osaka 560-0043, Japan
[22] Code 667, NASA Goddard Space Flight Center, Greenbelt, MD 20771, USA
[23] Zentrum für Astronomie der Universität Heidelberg, Astronomisches Rechen-Institut, Mönchhofstr. 12-14, 69120 Heidelberg, Germany
[24] Department of Physics, University of Auckland, Private Bag 92019, Auckland, New Zealand
[25] Department of Physics, The Catholic University of America, Washington, DC 20064, USA
[26] Institute of Space and Astronautical Science, Japan Aerospace Exploration Agency, 3-1-1 Yoshinodai, Chuo, Sagamihara, Kanagawa, 252-5210, Japan
[27] University of Canterbury Mt. John Observatory, P.O. Box 56, Lake Tekapo 8770, New Zealand